Nano Energy 83 (2021) 105828

Contents lists available at ScienceDirect

Nano Energy

journal homepage: http://www.elsevier.com/locate/nanoen

Solar steam generation on scalable ultrathin thermoplasmonic TiN nanocavity arrays

Luca Mascaretti [a,1], Andrea Schirato [b,c,1], Radek Zbořil [a,d], Štěpán Kment [a,d], Patrik Schmuki [e], Alessandro Alabastri [f,*], Alberto Naldoni [a,g,**]

[a] Regional Centre of Advanced Technologies and Materials, Faculty of Science, Palacký University, Šlechtitelů 27, 78371 Olomouc, Czech Republic
[b] Department of Physics, Politecnico di Milano, Piazza Leonardo da Vinci 32, 20133 Milan, Italy
[c] Istituto Italiano di Tecnologia, Via Morego 30, 16163 Genoa, Italy
[d] Nanotechnology Centre, VŠB–Technical University of Ostrava, 17. listopadu 2172/15, 708 00 Ostrava-Poruba, Czech Republic
[e] Department of Materials Science and Engineering, University of Erlangen-Nuremberg, Martensstrasse 7, D-91058 Erlangen, Germany
[f] Department of Electrical and Computer Engineering, Rice University, 6100 Main Street, 77005 Houston, TX, United States
[g] Institute of Fundamental and Frontier Sciences, University of Electronic Science and Technology of China, Chengdu 610054, China

ARTICLE INFO

Keywords:
Ultrathin plasmonic TiN absorber
Solar steam generation
Nanocavity array
Multi-physics modeling
Quasi-two dimensional heat transfer

ABSTRACT

Plasmonic-based solar absorbers exhibit complete light absorption in a sub-μm thickness, representing an alternative to mm-thick carbon-based materials most typically employed for solar-driven steam generation. In this work, we present the scalable fabrication of ultrathin plasmonic titanium nitride (TiN) nanocavity arrays that exhibit 90% broadband solar light absorption within ~ 250 nm from the illuminated surface and show a fast non-linear increase of performance with light intensity. At 14 Suns TiN nanocavities reach ~ 15 kg h^{-1} m^{-2} evaporation rate and ~ 76% thermal efficiency, a steep increase from ~ 0.4 kg h^{-1} m^{-2} and ~ 20% under 1.4 Suns. Electromagnetic, thermal and diffusion modeling of our system reveals the contribution of each material and reactor component to heat dissipation and shows that a quasi-two-dimensional heat dissipation regime significantly accelerates water evaporation. Our approach to ultrathin plasmonic absorbers can boost the performance of devices for evaporation/desalination and holds promise for a broader range of phase separation processes.

1. Introduction

The widespread availability and abundance of solar radiation as a renewable energy source have led to its application in diverse fields such as photovoltaics [1,2], hydrogen production [3], photocatalysis [4,5], solar-thermal conversion [6], and steam generation [7–9]. The latter, in particular, has recently emerged as a cost-effective solution for off-grid water desalination [10–12], distillation [13,14] and purification [13,15], with its potential implementation in remote locations thanks to simpler reactor designs compared to large-scale reverse osmosis desalination plants [7,16].

Solar steam generation involves light-to-heat conversion within a broadband absorber that, by increasing water temperature in its proximity, promotes the evaporation process. The so-obtained steam can be then collected, upon condensation, as clean water [7,8]. Ideally, solar absorbers feature large absorption coefficients to dissipate solar radiation in relatively thin layers, in contrast to mm-thick commercial black paints [17], thus minimizing the amount of required material and maximizing heat power density within the absorbers themselves. In the search of improved solar absorbers, various materials have been considered, such as plasmonic metal nanoparticles dispersed in liquid [14,18,19], or floating three-dimensional (3D) carbon- [11–13,20–23] and/or plasmonic-based [10,24–26] structures. The great interest in plasmonic materials is motivated by the efficient light-to-heat conversion upon the dissipation of plasmonic modes [27] (i.e., collective oscillations of conduction electrons in response to the incident

* Corresponding author.
** Corresponding author at: Regional Centre of Advanced Technologies and Materials, Faculty of Science, Palacký University, Šlechtitelů 27, 78371 Olomouc, Czech Republic.
E-mail addresses: alessandro.alabastri@rice.edu (A. Alabastri), alberto.naldoni@upol.cz (A. Naldoni).
[1] These authors contributed equally to this work.

https://doi.org/10.1016/j.nanoen.2021.105828
Received 16 December 2020; Received in revised form 12 January 2021; Accepted 23 January 2021
Available online 26 January 2021

electromagnetic field) that can be easily tuned by controlling the size and the chemical environment of plasmonic nanostructures [28–32]. Such a high efficiency of heat generation by plasmonic materials has indeed given rise to the sub-field of the so-called thermoplasmonics [33].

Plasmonic materials offer even more unique advantages in the form of ultrathin layers based on periodic arrays, i.e. the so-called quasi two-dimensional (2D) metamaterials or metasurfaces [34,35]. By carefully controlling the dimensional parameters of arrays of nanostructures in the sub-wavelength regime, the electromagnetic radiation can be manipulated in unusual ways, a technique that has led to scientific advancements in many optical devices [35–37]. Moreover, a 2D array of dissipative plasmonic nanostructures can effectively promote a substantial heating thanks to collective photothermal effects [38,39]. Ultrathin broadband solar absorbers with a thickness limited to ~ 100–200 nm have been realized employing plasmonic metamaterials [40–42]. Although solar absorbers based on periodic structures have been reported, such as anodic alumina oxide (AAO) coated by Au or TiN [10,24,26], a further reduction of the thickness down to the ~ 100 nm scale may lead to faster evaporation dynamics because of the increased power densities in the plasmonic metasurface layer. For example, by absorbing unfocused solar radiation (~ 1 kW m^{-2}) in a ~ 100 nm thick dissipating layer would yield to an average heat power density of ~ 10 GW m^{-3}. Such large power densities can trigger fast thermal processes in ultrathin devices, opening the possibility for exploiting nanoscale photothermal effects in large area systems. Here we experimentally demonstrate and numerically validate the efficacy of plasmonic metasurfaces in vaporizing water and we theoretically show how the process can be accelerated through nanoscale heat transfer.

2. Results and discussion

We propose an ultrathin solar absorber based on plasmonic titanium nitride (TiN), an emergent thermoplasmonic material alternative to gold thanks to its similar absorption spectrum, but also ~ 40 times cheaper and showing refractory nature, complementary metal oxides compatibility, and superior heat dissipation [41,43–46]. The TiN-based solar absorber (TSA) is enclosed within a thermally-insulating polytetrafluoroethylene (PTFE) cell having, in its top section, a cylindrical through-hole (1 cm diameter) working as basin to collect water, reminiscent of a solar still (Fig. 1A). Solar-simulated light is then focused at the top surface of the water collector (i.e. the light spot has a diameter of ~ 1 cm) to heat water and the TSA, driving the steam generation. The TSA consists of three different layers, as a result of the fabrication process (Fig. 1B, see also Supplemental Notes). The first layer is made of a TiN nanocavity array (Fig. 1C) with optimized thermoplasmonic properties for improved light-to-heat conversion [47]. The array is obtained by anodizing a commercial 125 μm-thick Ti foil in acidic solution, which leads to the self-organization of TiO_2 nanocavities in a hexagonal array [48,49], and then by nitridation in NH_3 atmosphere (see Experimental and Numerical Methods). The so-obtained TiN nanocavities exhibit a typical diameter of ~ 80 nm, height of ~ 180–200 nm, and center-to-center distance of ~ 100 nm (Fig. 1D) [47]. Anodization was employed as a scalable process to obtain nanostructures over cm-scale areas [50]. The nitridation process, on the other hand, leads to a stoichiometric TiN composition in the nanocavities, as confirmed by high-resolution transmission electron microscopy (HRTEM)-energy dispersive X-ray spectroscopy (EDS) elemental mapping (Fig. 1D) and X-ray diffraction (Fig. S1). The second layer is a Ti_2N layer of ~ 1 μm thickness, which is formed beneath the TiN nanocavities as a result of diffusion of NH_3 through the Ti plate (Fig. 1B). Finally, the third layer is the rest of the substrate, which remains in the form of metallic Ti (Fig. 1B). We employ finite element method (FEM)-based electromagnetic numerical simulations to show that the optical power absorption at visible wavelengths (Figs. 1E, 1F and S2) is actually confined in a thickness of ~ 250 nm, corresponding to the height of TiN nanocavities, while in the near IR region it increases to ~ 350 nm (Fig. S2). This is reflected by Fig. 1F, which shows that the modulus of the vertical component of the Poynting vector $|\mathbf{P}_z|$, quantifying the power flow through the structure, exhibits a rapid decay in the nanocavities height h_{TiN}. Such an efficient optical absorption and subsequent heat generation is attributed to the collective photothermal effects of the TiN

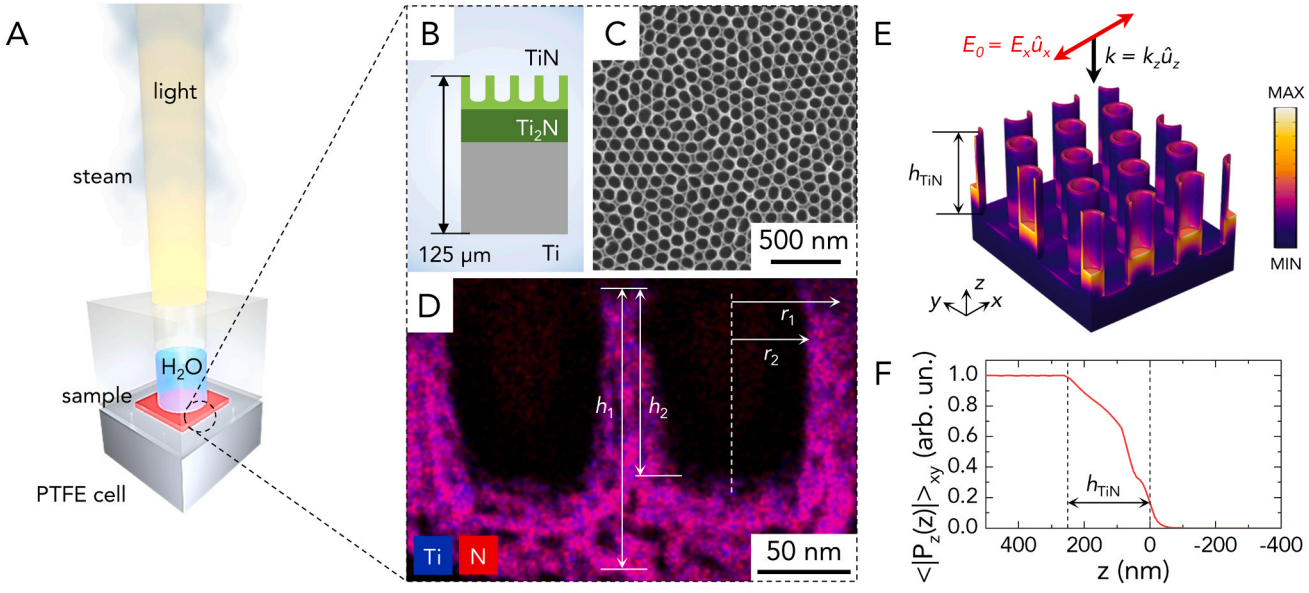

Fig. 1. Steam generation by the TSA. (A) Schematic of water evaporation and steam generation by the TSA under moderate light concentration in a custom-made PTFE cell. (B) Schematic structure of the TSA: TiN nanocavities (250 nm thickness), Ti_2N thermal layer (~ 1 μm), and rest of the Ti substrate. (C) Top-view SEM image of TiN nanocavities. (D) HRTEM-EDS elemental mapping for Ti (blue) and N (red). The panel also reports the geometrical parameters of the nanocavities: external height h_1, cavity depth h_2, external radius r_1, and internal radius r_2. (E) Simulated power absorption across the nanocavities array upon plane wave illumination (normal incidence with linearly-polarized electric field **E** along *x*-axis, exemplary excitation wavelength $\lambda = 500$ nm), computed following Joule dissipation. The electromagnetic power is then converted into heat following this same spatial pattern. (F) Modulus of the vertical component of the Poynting vector, $|\mathbf{P}_z|$, averaged over horizontal (*xy*) plane as a function of the direction normal to the structure (*z*-axis), shown for $\lambda = 500$ nm and normalized to its incident value.

nanocavity array [47]. As such, the TSA can be considered as a promising quasi-bidimensional absorber for efficient heat dissipation in confined volumes over large areas.

Due to the optically opaque nature of the TSA, the optical properties were evaluated by UV–visible-NIR spectroscopy in reflectance (R) mode, from which the absorption was retrieved as $A = 1–R$, being zero the transmittance (T). The experimental reflectance and absorption spectra in air are shown in Fig. 2A, together with their simulated counterparts (see Fig. S3 and Note S1 for the electromagnetic modeling of the TSA). These results clearly show the capability of TiN nanocavities to efficiently absorb the solar light in a broad range, which is the first requirement to achieve an efficient photothermal conversion and heat generation both in air and water environments, confirming previous studies on the same material [47]. The experimental overall absorption in air, weighted for the solar irradiance spectrum in the range 200–1100 nm, is ~ 90%, in good agreement with simulations (Fig. 2A). The slight mismatch between the experimental and the theoretical curves can be due to the fact that numerical simulations do not take into account neither size distribution effects of the nanocavities nor local imperfections in the hexagonal array [47]. Since the TSA is placed at the bottom of the water reservoir in the PTFE cell for steam generation experiments, its optical properties in water must be considered. In particular, the absorption spectrum in water was numerically simulated and the contributions of each layer constituting the TSA were disentangled (Fig. 2B and Fig. S3): the TiN nanocavities layer (green), a 100-nm thick Ti layer beneath them (cyan), and the further substrate (blue). Consistently with previous investigations [47], optical simulations did not explicitly include the Ti_2N layer due to its similar electronic properties to TiN (see also Note S1) [51]. As a first remark, the overall absorption in water is very similar to that in air in the range 300–800 nm, after which the former drops to values < 80% due to the increasing absorption coefficient of water in the IR region [52]. Moreover, by evaluating dissipation spectra separately, it was possible to ascribe spectral features of the total absorption to the different components of the TSA. In the UV–visible range, light absorption is efficiently confined within the TiN nanocavities layer, in agreement to the results of Fig. 1E and F. At $\lambda > 800$ nm, conversely, the substrate has a crucial role in maintaining the total absorption above 65%. Interestingly, a substantial contribution is given by a 100 nm-thick Ti underlayer under TiN, while all the remaining Ti substrate only gives ~ 5% absorption at $\lambda > 1800$ nm. In other words, almost all the optical absorption of solar radiation within the TSA occurs in the first few hundreds of nm, i.e., in the TiN nanocavities and the immediate Ti underlayer. Light absorption in TiN nanocavities is affected by the excitation of plasmonic modes, as illustrated by the simulated spatial maps of electric field enhancement across a single nanocavity (Fig. 2C). In particular, at $\lambda = 500$ nm the absorption is due to pure cavity modes [53,54], resulting in the electric field mainly concentrated in the hollow core. At $\lambda = 1700$ nm, on the other hand, the absorption is related to the localized surface plasmon resonance (LSPR) at the cavity corners, producing an electric field enhancement mostly concentrated at the external surface of the cavities [47].

The solar steam generation performance of the TSA was evaluated by a custom-made setup, in which the PTFE cell enclosing the TSA, 800 mg of water and a thermocouple were placed on a high-precision balance and illuminated by solar-simulated light with various intensities (see Experimental and Numerical Methods and Fig. S4 for further details). Water evaporation experiments under light irradiation were run for 25 min, while no appreciable water evaporation was measured in the dark. Each TSA sample was tested several times over a period of few months showing stable performance after several runs of water evaporation. Fig. 3A shows the time-dependent experimental and simulated evaporation rate for the TSA under 1.4–9.8 Suns (see below for more details on the simulations). The time-dependent evaporation rate $\dot{m}(t)$ (kg h^{-1} m^{-2}) was calculated from the mass change Δm (Fig. S5) for each specific time interval Δt by the formula $\dot{m}(t) = \Delta m/\Delta t$. It is possible to observe a monotonic increase of the evaporation rate with time because of the variation in the slope of the mass change (Fig. S5), and with the incident light intensity (from ~ 0.4 kg h^{-1} m^{-2} at 1.4 Suns to ~ 5.5 kg h^{-1} m^{-2} at 9.8 Suns). Moreover, we found a good agreement between the experimental and calculated curves. Only for the case at 9.8 Suns a mismatch occurs (evaporation rate ~ 4.4 kg h^{-1} m^{-2}), which is ascribed to the limitations of the numerical model in reproducing the phenomenon of boiling and bubble formation (see Note S2). Bubbles were indeed observed at high irradiation conditions, but their origin (either steam or air) could not be identified. For the same reason, no simulations were performed for the highest irradiation conditions (12.6 and 14 Suns). In addition, it is possible to note that the evaporation rate reaches a relatively stable value only for the lowest irradiation condition (1.4 Suns), meaning that in our experimental conditions no steady state could be achieved, likely due to the limited (800 μL) and continuously decreasing volume of water in the PTFE cell. The corresponding temperatures measured in water slightly above the TSA surface are reported in Fig. 3B, ranging from ~ 37 °C at 1.4 Suns to ~ 96 °C at 9.8 Suns. Also in this case it is possible to appreciate a good agreement between the experimental and the numerical data. The slight underestimation of the simulations compared to experiments could be accounted for the additional temperature rise induced in the thermocouple by the solar-simulated light. The evaporation rate and the temperature profiles vs. time for water alone, without TSA, are instead reported in Fig. 3C and D, respectively. As expected, both the evaporation rates (maximum ~ 1.5 kg h^{-1} m^{-2} at 9.8 Suns) and the temperatures (maximum ~ 75 °C

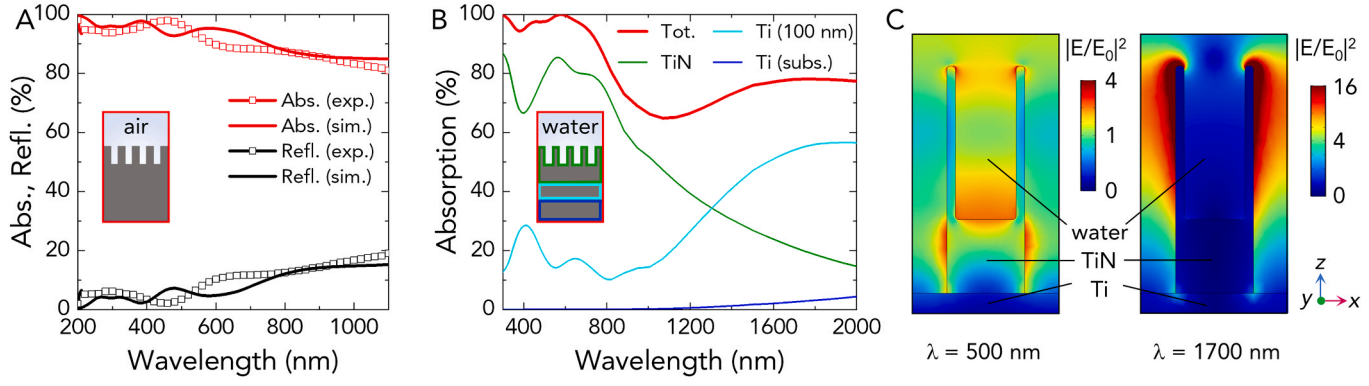

Fig. 2. Optical properties of the TSA. (A) Experimental (symbols) and simulated (solid lines) absorption (red) and reflectance (black) of the TSA in air. (B) Simulated absorption of the TSA in water (red), disentangled in terms of contributions arising from the TiN nanocavities (green), the 100 nm-thick Ti underlayer (cyan), and the Ti substrate (blue). (C) Spatial maps of electric field enhancement across a single TiN nanocavity, numerically computed at $\lambda = 500$ nm (left) and $\lambda = 1700$ nm (right).

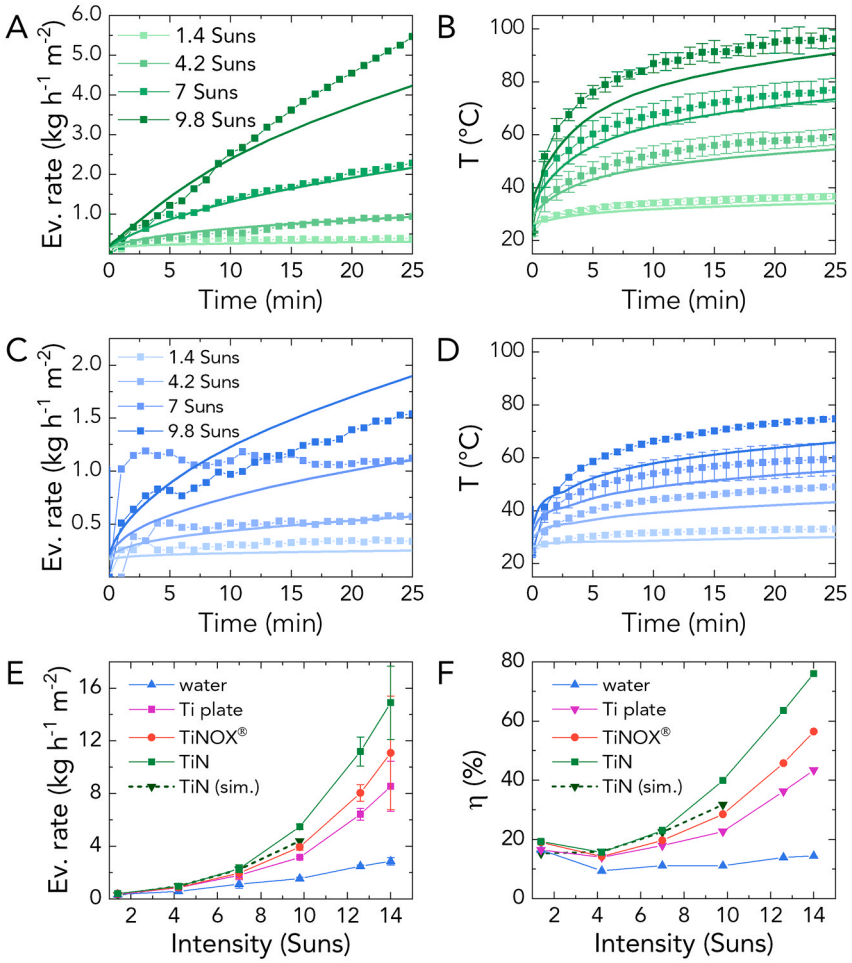

Fig. 3. Solar-driven steam generation by the TSA. (A and B) Time-dependent water evaporation rate with the TSA (A) and corresponding temperatures (B) under different light intensities (symbols: experimental; solid lines: simulated). (C and D) Same as (A and B), respectively, but without the TSA. (E and F) Water evaporation rate and corresponding solar-to-vapor conversion efficiency, respectively, under different light intensities for different materials, evaluated at $t = 25$ min; for TiN, the simulated data are also included (dark green dashed line).

at 9.8 Suns) are lower than those measured in the presence of the TSA, especially at higher irradiation conditions (i.e. 7 and 9.8 Suns). Conversely, at low irradiation conditions (especially at 1.4 Suns), light from the solar simulator is mostly absorbed in the water volume close to the upper surface of the reservoir, thus accounting for the similarity with the data in Fig. 3A and B. The small deviation between experimental and numerical curves, in the case of water only (Fig. 3C and D) is observed at short times only, where evaporation rates tend to exhibit a less reliable trend.

An overview of all the experimental evaporation rates in all the investigated irradiation conditions is reported in Fig. 3E. This figure not only reports the data for the TSA (both measured and simulated) and for water, but also for a Ti plate (i.e., the substrate on which TiN nanocavities were grown) and for a commercial solar absorber material as benchmark for solar-thermal applications. The latter consisted in a multilayer metallic spectrally-selective absorber, TiNOX®, in which the solar absorber layer is a cermet structure. It is possible to note that, while at 1.4 Suns the evaporation rates for all the cases are almost the same (~ 0.3–0.4 kg h^{-1} m^{-2}), their values spread by increasing the light intensity. In particular, a non-linear increase of the evaporation rate and efficiency was found, consistently with previous studies [11], and the maximum value was achieved by the TSA at 14 Suns (~ 14.9 kg h^{-1} m^{-2}). Notably, the TSA outperformed the Ti plate, i.e. the substrate itself (~ 8.5 kg h^{-1} m^{-2}), but also the commercially available TiNOX® (~ 11.1 kg h^{-1} m^{-2}), positioning the TSA as a promising candidate for large-scale ultrathin absorbers. Additional solar steam generation experiments featuring a TSA covering a ten times higher surface area than before confirmed the role of plasmonic enhancement in the water evaporation process, reaching similar performances to those obtained with the small-scale PTFE reactor (Fig. S6). Detailed theoretical insights on the scalability of the TSA are reported in the Supporting Information (Fig. S7 and Note S3).

The non-linear increase of the evaporation rate with the TSA (+ 3700% from 1.4 to 14 Suns, Fig. 3E) is higher than the linear increase typically reported in previous studies concerning plasmonic absorbers (Fig. S8A) [10,24,25,55,56]. In particular, at low irradiation conditions other systems showed a higher evaporation rate, such as anodic alumina oxide membranes combined with Al [10], Au [24] or HfN [55] nanoparticles, likely due to the interfacial configuration arrangement. However, since in those cases the evaporation rate increased linearly (e.g. + 1570% for black Au film from 1 Sun to 13 Suns) [25], our system showed a better performance at moderate light concentrations. For example, even under 17 Suns the black Au film [25] showed an evaporation rate of ~ 13 kg h^{-1} m^{-2}, lower than that of the TSA at 14 Suns (Fig. S8A). The non-linear increase found here could be related to the exponential (Beer-Lambert-like) increase of light penetration through the water layer above the TSA and to the exponential increase of the saturation vapor pressure of water with temperature [11].

The evaporation efficiency (η) was calculated by the following formula [7,20]:

$$\eta = \frac{\dot{m} h_{LV}}{C_{opt} q_i} \quad (1)$$

where $\dot{m}$ is the evaporation rate (calculated at the end of the experiments), h_{LV} is the total enthalpy of liquid-vapor phase change (kJ kg^{-1}), C_{opt} is a concentration factor (from 1.4 to 14), and $q_i = 1$ kW m^{-2} = 1 Sun is the nominal solar flux. The term h_{LV}, in particular, was calculated

as [7]

$$h_{LV} = c_{H_2O}\Delta T + h_{fg} \quad (2)$$

where $c_{H_2O} = 4.186$ kJ kg^{-1} K^{-1} is the specific heat capacity of water at constant pressure (which negligibly changes in the temperature range 0–100 °C), ΔT is the temperature change from the beginning to the end of the experiment, and h_{fg} is the latent heat of vaporization (kJ kg^{-1}), whose temperature dependence was instead taken into account by an empirical polynomial equation [57]. The data for all the investigated conditions are accordingly reported in Fig. 3F, as well as for the simulated TSA up to 9.8 Suns. As in Fig. 3E, the values at 1.4 Suns are similar for all the samples, with efficiencies falling in the range 16–19%. By increasing the light intensity, an initial drop at 4.2 Suns is observed probably due to optical losses related to light concentration [20,25] and to the baseline evaporation rate (Fig. S9), while at higher solar intensities the efficiency remained almost constant for water (from ~ 11% to ~ 14%) and increased when a solar absorber was employed. In particular, for the TSA the efficiency ranged from ~ 15.6% at 4.2 Suns to ~ 76% at 14 Suns, outperforming TiNOX® (maximum η ~ 56%) and the Ti plate (maximum η ~ 43%). In addition, the simulated efficiency for the TSA was in good agreement with the experimental one up to 7 Suns. Despite the relatively low efficiency values for the TSA at low irradiation condition, likely due to the TSA location far from the water surface, a remarkable ~ 4-fold efficiency improvement by increasing the light intensity from 1.4 to 14 Suns was found (Fig. 3F). Other plasmonic-based absorbers showed higher efficiencies in interfacial configuration [10,24,25,55,56] (e.g. η ~ 99% for anodic alumina membranes filled with HfN at 4 Suns [55], Fig. S8B), which indeed is more suitable to reach higher performances due to the efficient heat localization at the liquid surface [7,8]. Such a configuration was, however, not feasible in this work due to the non-floating and non-porous nature of the Ti substrate on which TiN nanocavities were prepared. Nevertheless, other 2D plasmonic arrays based on Au have shown fifty-times smaller increase compared to TSA (e.g. only + 3% for black Au film from 1 Sun to 13 Suns [25], Fig. S8B).

The simulations of the TSA-assisted steam generation experiments (Fig. 3) were achieved by a comprehensive multiphysics and multi-scale thermo-fluid modeling of all the interlinked phenomena involved in the evaporation process, i.e., optical absorption, heat generation and transport, fluid dynamics, and photon scattering. This model is schematized in Fig. 4A, while Supporting Information reports additional details regarding the geometry of the model itself (Fig. S10) and typical results for the temperature distribution (Fig. S11), convective flows in the water reservoir (Fig. S12), and water vapor concentration in the surrounding air (Fig. S13). A thorough discussion of the model is reported in Note S2. Schematically, Fig. 4A shows that radiation coming from the solar simulator and focused by the Fresnel lens impinges on the water volume on top of the TSA, the two surrounded by PTFE. Considering that light absorption in the TSA mostly occurred in the TiN nanocavities and in the thin Ti underlayer (Fig. 2B), only these two layers were considered as dissipaters in the TSA region. The dissipation in water was taken into account by weighing its wavelength dependent absorption coefficient over the solar spectrum (see also Fig. S10 and Note S2). Moreover, the spatial arrangement of TiN nanofurnaces was neglected and the TiN layer was considered as a homogeneous 250 nm-thick layer. From the heat dissipation point of view, indeed, any spatial inhomogeneity of sub-μm-thick dissipaters can be neglected when the dimensions of the adjacent domains (i.e., the water volume and the PTFE cell) are orders of magnitude larger (see Fig. S14 and Note S4 for a more detailed description) [39]. Moreover, due to the large light scattering provided by PTFE, the cell effectively concentrates the incoming radiation in the active area additionally to its thermal insulation role, resulting in a higher solar intensity reaching the TSA surface. The paths of few exemplary photons were calculated through a Monte Carlo based approach within the PTFE and are sketched in Fig. 4A, depicting the randomizing effect of PTFE on the photon propagation direction (see Fig. S15 and Note S5). Due to the non-trivial paths of photons, radiation dissipation is modified in the whole structure, resulting in a more complex heat source distribution for the thermal model describing the experimental system. A further heat source due to the non-negligible lens heating was included as well (Note S2).

Beyond the time-dependent numerical results shown in Fig. 3, the model was employed to predict the system performances in the stationary regime as well. Such regime could not be tested experimentally due to the complete evaporation of water at longer times. A

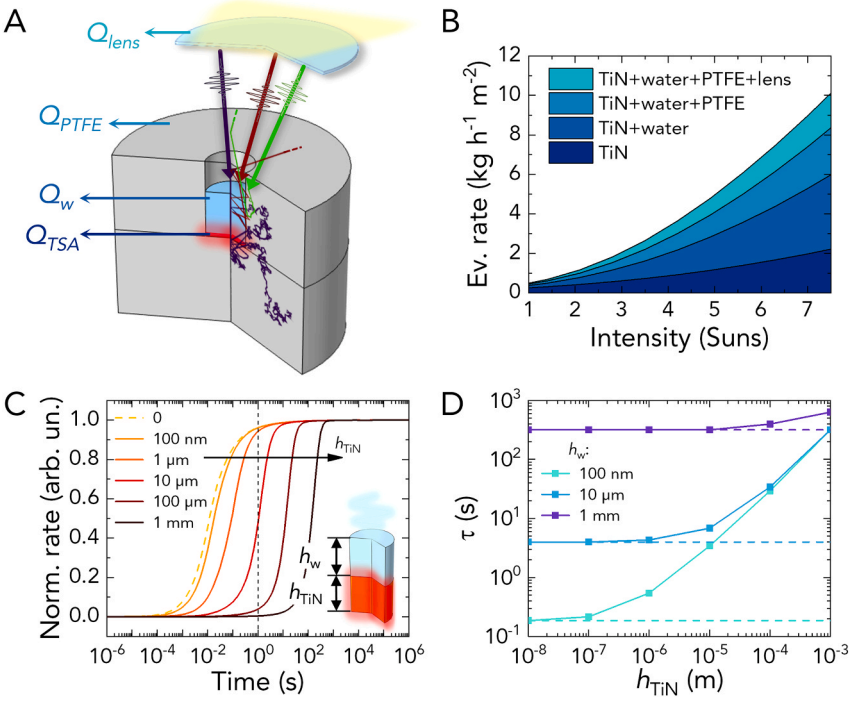

Fig. 4. Modeling of TSA-assisted steam generation. (A) Schematic of the thermal modeling of the experimental setup, where the paths of few exemplary photons within the scattering PTFE cell are shown. Heat sources included in the modeling are also highlighted. (B) Simulated evaporation rate in stationary regime, disentangled in terms of the dissipation contributions due to single heat sources. (C) Evaporation rates normalized to the stationary value computed in a simplified model (see right inset) for a 100 nm-thick water layer and varying TiN thickness (h_{TiN}), from 0 (limit case of surface heating) to 1 mm. The vertical dashed line marks the time $t = 1$ s. (D) Characteristic time τ the system, as in (C), takes to reach the steady state, as a function of h_{TiN} for different h_w: 100 nm, 10 μm and 1 mm. The dashed lines represent the zero-thickness limit scenario for a fixed h_w.

disentanglement of heating contributions was also performed to distinguish the terms related to different dissipating elements. The simulated steady-state evaporation rates as a function of light intensity associated to the individual components of the experimental setup are reported in Fig. 4B. Numerical predictions clearly show to what extent each component has a role in the evaporation process. Clearly, the main contributions are associated to TiN and water. Nevertheless, the radiation confinement produced by the PTFE cell (Fig. S15) and the additional heating induced by the Fresnel lens further contribute to the evaporation process promoted by the TSA, resulting in the evaporation rates experimentally measured (Fig. 3).

Furthermore, we numerically investigated the time needed to reach the stationary state for water evaporation (Fig. 4C) moving from 3D heat transfer conditions to a quasi-2D scenario, in which the confined dissipation in the ultrathin TSA can be fully revealed. While the full geometrical features of a metasurface should be considered when the water layer thickness h_w becomes comparable to the TiN layer thickness h_{TiN}, here we employed a simplified model to highlight the time dependent heat transfer properties of different layers spanning size over orders of magnitude. Our model is composed of a passive water layer on top of an active TiN layer (inset of Fig. 4C and Fig. S16), the latter characterized by the same thermal properties as the TiN layer in the previous model (see Note S6 for further details). The radius of both TiN and water layers is 0.5 cm. The system is considered insulated on its lateral walls but can exchange heat by conduction and vaporization through the water/air interface. We studied the dependence of the evaporation rate, normalized to its stationary value, for $h_w = 100$ nm and varying values of h_{TiN}, from 1 mm to 0 thickness, which represents the limiting case of surface heating dissipating 1 Sun. For each other thickness, the heat dissipation density has been set to 1 kW m^{-2} / h_{TiN}, thus maintaining constant the total input power. The time dependent evaporation dynamics is shown in Fig. 4C. While the curves follow similar trends, the timescale strongly depends on the TiN layer thickness. Thinner layers imply faster thermalization, as expected by heat dynamics at smaller scales. Interestingly, the case $h_{TiN} = 100$ nm is virtually equivalent to the 0 nm limit case where pure surface heating is considered. This observation shows how thin plasmonic metasurfaces can indeed accelerate thermal processes. In Fig. 4D we report the thermalization times (the time required to reach 90% of the steady state evaporation rate), τ, for h_{TiN} spanning from 10 nm to 1 mm in the case of three different layers of water: 100 nm, 10 μm and 1 mm. As expected, the larger the overall system (TiN+water), the longer it takes for reaching steady state. However, the plot clearly shows how sub-μm absorbers are required if water thicknesses below ~ 10 μm are considered. For example, only a few tenths of seconds are required to thermalize a system with $h_{TiN} = 100$ nm and $h_w = 100$ nm, compared to the hundreds of seconds a combination with $h_{TiN} = 1$ mm and $h_w = 100$ nm would require. Moreover, it should be noticed that such thermalization times are calculated for a relatively large $w = 1$ cm diameter system. Since τ is expected to decrease with the volume of the heated system, for given layer thicknesses we can infer $\tau \propto w^2$. Therefore, even faster dynamics are expected if smaller scales can be managed, depending on the intended application. This observation suggests the great promise plasmonic metasurfaces hold in accelerating thermal processes beyond steam generation, such as phase changes or Arrhenius-type chemical reactions, within light driven micro/nanofluidics devices. The fast thermalization may also allow the use of non-continuous irradiation, paving the way to the study of nanoscale thermal processes under pulsed or intermittent illumination.

3. Conclusion

In summary, we introduced an ultrathin solar absorber based on TiN nanocavities and demonstrated its thermoplasmonic properties in solar steam generation experiments. The periodic array of nanocavities was easily achieved by a scalable method, based on anodization and thermal nitridation, ensuring a broadband light absorption confined in few hundreds of nm in thickness thanks to plasmonic and cavity resonances. Efficient steam generation under moderate light concentration was achieved with an evaporation rate of ~ 15 kg h^{-1} m^{-2} and efficiency of ~ 76% at 14 Suns, outperforming commercially available solar absorbers and showing a higher and non-linear performance enhancement compared to other cases in the literature. A comprehensive electromagnetic and thermal modeling of the involved materials and of the overall experimental system, including a light diffusing thermally-insulating PTFE cell, revealed the substantial light absorption confinement in the TiN nanocavities. This effect confined the heat dissipation volume at the surface layer of the absorber. Further light concentration was found to be due to photon scattering within the PTFE cell. Such multiphysics thermo-fluid modeling successfully reproduced the experimental steam generation data and was further employed to study the transition from 3D to 2D heat transfer regime, demonstrating the acceleration by up to two orders of magnitude of the evaporation process in case of a sub-μm thickness of both the TiN absorber and water overlayer. The outcome of simulations thus provides a guidance to further improve the performance of the ultrathin TiN-based solar absorber, not only by engineering the components of the reactor, but also adjusting the thickness of the absorber itself and of water. Our work opens to fast water evaporation dynamics, which is relevant not only for solar steam generation, but also for nano-optofluidics, confined chemical reactions, sensing, fast phase separation, and smart surfaces.

4. Experimental and numerical methods

4.1. Samples preparation

TiN nanocavities were prepared according to the procedure reported in a previous work [47]. Briefly, 125-μm thick Ti plates (Goodfellow, England) were anodized to form TiO_2 nanocavities in a two-electrode electrochemical cell (Pt counter electrode) in a HF/H_3PO_4 solution [48,49] and, upon drying, thermally treated at 600 °C in NH_3 to convert them to TiN. Ti plate and TiNOX® Energy (Almeco GmbH, Germany) were cut in ~ 1.5 × 1.5 cm^2 pieces and ultrasonically cleaned in acetone, ethanol and deionized water before experiments.

4.2. Materials characterization

The morphology of the studied materials was investigated by scanning electron microscopy (SEM, Hitachi FE-SEM 4800) and high-resolution transmission electron microscopy (HRTEM, Titan G2). The chemical composition was analyzed by energy-dispersive X-ray spectroscopy (EDS) in scanning TEM mode (STEM) using the Super-X system with four silicon drift detectors (Bruker). STEM images were taken with a high-angle annular dark-field imaging (HAADF) detector (Fischione, model 3000). TEM lamella was prepared with a FEI Helios Focused Ion Beam/SEM (Thermo Scientific).

The crystalline structure of the studied materials was investigated by X-ray diffraction (XRD) using a high-resolution X-ray powder diffractometer (PANalytical X'Pert Pro MPD) with Co Kα radiation (λ = 0.1789 nm). The measurements were performed in grazing incidence geometry (ω = 3.6°) in a 2θ range of 25–85° with a step size of 0.016° and a time step of 40 s.

The optical properties of the materials in air were investigated by reflectance spectra measured with a Specord®250 Plus spectrometer equipped with an integrating sphere (Analytik Jena GmbH).

4.3. Numerical simulations

A multiphysics and multiscale approach was necessary to account for all phenomena triggered by Sun-like illumination and inducing water-to-vapor conversion. A finite-element-method (FEM) based model was developed using a commercial software (COMSOL Multiphysics 5.4) to

simulate all processes occurring in the experimental system. First, a full-vectorial three-dimensional electromagnetic problem was numerically set to estimate the absorption of radiation in a hexagonal array of TiN nanocavities. With this information at the nanoscale, light-induced dissipation in the macroscale sample was evaluated and the thermal modeling of the experimental structure was subsequently addressed. To do so, a simulation coupling laminar flows (for the natural convection in water and air), diffusion (for the water vapor concentration at the water/air interface) and thermal transport (for the heating of the whole structure) was settled. Dissipation contributions produced in the TSA sample itself, water, the PTFE cell, and the lens, respectively, upon Sun-like illumination were accounted for. Moreover, due to the highly scattering nature of the PTFE cell, a thorough estimation of the actual amount of radiation exciting each component was necessary. Thus, a FEM-based Monte Carlo-like approach was developed to quantify, on the one hand, the percentage of incoming photons which effectively excite the TiN nanostructures, and, on the other hand, the effective length of the average trajectory of photons in the water reservoir. A detailed discussion of the modeling approach pursued in each of its part is reported in the Supporting Information (Notes S1–S6).

4.4. Water evaporation experiments

The reactor consisted in a PTFE cell made of two parts to allow a firm positioning and an efficient thermal insulation of the sample: a top part ($4.4 \times 4.7 \times 1.7$ cm^3) with a 1 cm-diameter through-hole in the middle, as cylindrical water reservoir, and a bottom part ($4.4 \times 4.7 \times 2.0$ cm^3). The sample was centered along the water container and positioned in the PTFE cell, together with a type K thermocouple (RS PRO, 0.075 mm diameter). The PTFE cell was then placed on a high-precision analytical balance (Kern & Sohn GmbH, 0.1 mg accuracy) and 800 μL (800 mg) of deionized water were inserted in the water reservoir. Afterwards, light irradiation was provided by a 1000 W solar simulator (Sciencetech A4 Lightline C250) equipped with an AM 1.5 G filter and the light spot was focused with a Fresnel lens (Thorlabs FRP251) on the top surface of the PTFE cell to match the diameter of the water reservoir. The light intensity was measured prior to experiments by a thermopile power meter (Standa 11UP19K-30 H-H5).

CRediT authorship contribution statement

Luca Mascaretti: Methodology, Validation, Investigation, Writing - original draft. **Andrea Schirato:** Methodology, Software, Investigation, Writing - original draft. **Radek Zbořil**: Resources, Funding acquisition; **Štepán Kment**: Resources, Funding Acquisition. **Patrik Schmuki:** Resources, Supervision, Funding acquisition. **Alessandro Alabastri:** Conceptualization, Methodology, Software, Resources, Writing - review & editing, Supervision, Project administration, Funding acquisition. **Alberto Naldoni:** Conceptualization, Methodology, Resources, Writing - review & editing, Supervision, Project administration, Funding acquisition.

Declaration of Competing Interest

The authors declare the following financial interests/personal relationships which may be considered as potential competing interests: Some authors are coinventors on the provisional patent application relating to the research presented in this paper.

Acknowledgments

The authors gratefully acknowledge support of the Ministry of Education, Youth and Sports of the Czech Republic (MEYS CR) through the project ERC CZ no. LL1903 and the Operational Programme Research, Development and Education – European Regional Development Fund, project no. CZ.02.1.01/0.0/0.0/15_003/0000416. This material is based upon work supported by the National Science Foundation under Grant No. (IIP-1941227). The authors also thank Fabrizio Naldoni for the fabrication of the PTFE cell, Ondřej Tomanec for TEM and EDS measurements, Seyyedmohammadhossein Hejazi for XRD measurements, and Almeco GmbH (Germany) for providing TiNOX® Energy samples. The authors acknowledge CzechNanoLab Research Infrastructure supported by MEYS CR (LM2018110).

Appendix A. Supporting information

Supplementary data associated with this article can be found in the online version at doi:10.1016/j.nanoen.2021.105828.

References

[1] C. Battaglia, A. Cuevas, S.D. Wolf, High-efficiency crystalline silicon solar cells: status and perspectives, Energy Environ. Sci. 9 (2016) 1552–1576, https://doi.org/10.1039/C5EE03380B.
[2] L. Kavan, Electrochemistry and perovskite photovoltaics, Curr. Opin. Electrochem. 11 (2018) 122–129, https://doi.org/10.1016/j.coelec.2018.10.003.
[3] S. Ardo, D.F. Rivas, M.A. Modestino, V.S. Greiving, F.F. Abdi, E.A. Llado, V. Artero, K. Ayers, C. Battaglia, J.-P. Becker, D. Bederak, A. Berger, F. Buda, E. Chinello, B. Dam, V.D. Palma, T. Edvinsson, K. Fujii, H. Gardeniers, H. Geerlings, S.M. H. Hashemi, S. Haussener, F. Houle, J. Huskens, B.D. James, K. Konrad, A. Kudo, P. P. Kunturu, D. Lohse, B. Mei, E.L. Miller, G.F. Moore, J. Muller, K.L. Orchard, T. E. Rosser, F.H. Saadi, J.-W. Schüttauf, B. Seger, S.W. Sheehan, W.A. Smith, J. Spurgeon, M.H. Tang, R. van de Krol, P.C.K. Vesborg, P. Westerik, Pathways to electrochemical solar-hydrogen technologies, Energy Environ. Sci. 11 (2018) 2768–2783, https://doi.org/10.1039/C7EE03639F.
[4] Q. Wang, K. Domen, Particulate photocatalysts for light-driven water splitting: mechanisms, challenges, and design strategies, Chem. Rev. 120 (2020) 919–985, https://doi.org/10.1021/acs.chemrev.9b00201.
[5] B. Ohtani, Photocatalysis A to Z—what we know and what we do not know in a scientific sense, J. Photochem. Photobiol. C 11 (2010) 157–178, https://doi.org/10.1016/j.jphotochemrev.2011.02.001.
[6] L.A. Weinstein, J. Loomis, B. Bhatia, D.M. Bierman, E.N. Wang, G. Chen, Concentrating solar power, Chem. Rev. 115 (2015) 12797–12838, https://doi.org/10.1021/acs.chemrev.5b00397.
[7] P. Tao, G. Ni, C. Song, W. Shang, J. Wu, J. Zhu, G. Chen, T. Deng, Solar-driven interfacial evaporation, Nat. Energy 3 (2018) 1031–1041, https://doi.org/10.1038/s41560-018-0260-7.
[8] L. Zhu, M. Gao, C.K.N. Peh, G.W. Ho, Recent progress in solar-driven interfacial water evaporation: advanced designs and applications, Nano Energy 57 (2019) 507–518, https://doi.org/10.1016/j.nanoen.2018.12.046.
[9] H. Liu, Z. Huang, K. Liu, X. Hu, J. Zhou, Interfacial solar-to-heat conversion for desalination, Adv. Energy Mater. 9 (2019), 1900310, https://doi.org/10.1002/aenm.201900310.
[10] L. Zhou, Y. Tan, J. Wang, W. Xu, Y. Yuan, W. Cai, S. Zhu, J. Zhu, 3D self-assembly of aluminium nanoparticles for plasmon-enhanced solar desalination, Nat. Photon. 10 (2016) 393–398, https://doi.org/10.1038/nphoton.2016.75.
[11] P.D. Dongare, A. Alabastri, O. Neumann, P. Nordlander, N.J. Halas, Solar thermal desalination as a nonlinear optical process, Proc. Natl. Acad. Sci. (2019), 201905311, https://doi.org/10.1073/pnas.1905311116.
[12] X. Li, W. Xu, M. Tang, L. Zhou, B. Zhu, S. Zhu, J. Zhu, Graphene oxide-based efficient and scalable solar desalination under one sun with a confined 2D water path, Proc. Natl. Acad. Sci. 113 (2016) 13953–13958, https://doi.org/10.1073/pnas.1613031113.
[13] P.D. Dongare, A. Alabastri, S. Pedersen, K.R. Zodrow, N.J. Hogan, O. Neumann, J. Wu, T. Wang, A. Deshmukh, M. Elimelech, Q. Li, P. Nordlander, N.J. Halas, Nanophotonics-enabled solar membrane distillation for off-grid water purification, Proc. Natl. Acad. Sci. 114 (2017) 6936–6941, https://doi.org/10.1073/pnas.1701835114.
[14] O. Neumann, A.D. Neumann, S. Tian, C. Thibodeaux, S. Shubhankar, J. Müller, E. Silva, A. Alabastri, S.W. Bishnoi, P. Nordlander, N.J. Halas, Combining solar steam processing and solar distillation for fully off-grid production of cellulosic bioethanol, ACS Energy Lett. 2 (2017) 8–13, https://doi.org/10.1021/acsenergylett.6b00520.
[15] X. Zhou, F. Zhao, Y. Guo, B. Rosenberger, G. Yu, Architecting highly hydratable polymer networks to tune the water state for solar water purification, Sci. Adv. 5 (2019), eaaw5484, https://doi.org/10.1126/sciadv.aaw5484.
[16] J. Kim, K. Park, D.R. Yang, S. Hong, A comprehensive review of energy consumption of seawater reverse osmosis desalination plants, Appl. Energy 254 (2019), 113652, https://doi.org/10.1016/j.apenergy.2019.113652.
[17] J. Coventry, P. Burge, Optical properties of Pyromark 2500 coatings of variable thicknesses on a range of materials for concentrating solar thermal applications, AIP Conf. Proc. 1850 (2017), 030012, https://doi.org/10.1063/1.4984355.
[18] O. Neumann, A.S. Urban, J. Day, S. Lal, P. Nordlander, N.J. Halas, Solar vapor generation enabled by nanoparticles, ACS Nano 7 (2013) 42–49, https://doi.org/10.1021/nn304948h.
[19] N.J. Hogan, A.S. Urban, C. Ayala-Orozco, A. Pimpinelli, P. Nordlander, N.J. Halas, Nanoparticles heat through light localization, Nano Lett. 14 (2014) 4640–4645, https://doi.org/10.1021/nl5016975.

[20] H. Ghasemi, G. Ni, A.M. Marconnet, J. Loomis, S. Yerci, N. Miljkovic, G. Chen, Solar steam generation by heat localization, Nat. Commun. 5 (2014), 4449, https://doi.org/10.1038/ncomms5449.
[21] N. Xu, X. Hu, W. Xu, X. Li, L. Zhou, S. Zhu, J. Zhu, Mushrooms as efficient solar steam-generation devices, Adv. Mater. 29 (2017), 1606762, https://doi.org/10.1002/adma.201606762.
[22] M. Zhu, Y. Li, G. Chen, F. Jiang, Z. Yang, X. Luo, Y. Wang, S.D. Lacey, J. Dai, C. Wang, C. Jia, J. Wan, Y. Yao, A. Gong, B. Yang, Z. Yu, S. Das, L. Hu, Tree-inspired design for high-efficiency water extraction, Adv. Mater. 29 (2017), 1704107, https://doi.org/10.1002/adma.201704107.
[23] H. Liu, C. Chen, G. Chen, Y. Kuang, X. Zhao, J. Song, C. Jia, X. Xu, E. Hitz, H. Xie, S. Wang, F. Jiang, T. Li, Y. Li, A. Gong, R. Yang, S. Das, L. Hu, High-performance solar steam device with layered channels: artificial tree with a reversed design, Adv. Energy Mater. 8 (2018), 1701616, https://doi.org/10.1002/aenm.201701616.
[24] L. Zhou, Y. Tan, D. Ji, B. Zhu, P. Zhang, J. Xu, Q. Gan, Z. Yu, J. Zhu, Self-assembly of highly efficient, broadband plasmonic absorbers for solar steam generation, Sci. Adv. 2 (2016), e1501227, https://doi.org/10.1126/sciadv.1501227.
[25] K. Bae, G. Kang, S.K. Cho, W. Park, K. Kim, W.J. Padilla, Flexible thin-film black gold membranes with ultrabroadband plasmonic nanofocusing for efficient solar vapour generation, Nat. Commun. 6 (2015), 10103, https://doi.org/10.1038/ncomms10103.
[26] M. Kaur, S. Ishii, S.L. Shinde, T. Nagao, All-ceramic solar-driven water purifier based on anodized aluminum oxide and plasmonic titanium nitride, Adv. Sustain. Syst. 3 (2019), 1800112, https://doi.org/10.1002/adsu.201800112.
[27] H.H. Richardson, M.T. Carlson, P.J. Tandler, P. Hernandez, A.O. Govorov, Experimental and theoretical studies of light-to-heat conversion and collective heating effects in metal nanoparticle solutions, Nano Lett. 9 (2009) 1139–1146, https://doi.org/10.1021/nl8036905.
[28] U. Kreibig, M. Vollmer, Optical Properties Of Metal Clusters, Springer, Germany, 1995.
[29] S.A. Maier, Plasmonics: Fundamentals and Applications, Springer Science & Business Media, Germany, 2007.
[30] J.A. Schuller, E.S. Barnard, W. Cai, Y.C. Jun, J.S. White, M.L. Brongersma, Plasmonics for extreme light concentration and manipulation, Nat. Mater. 9 (2010) 193–204, https://doi.org/10.1038/nmat2630.
[31] A. Naldoni, V.M. Shalaev, M.L. Brongersma, Applying plasmonics to a sustainable future, Science 356 (2017) 908–909, https://doi.org/10.1126/science.aan5802.
[32] E. Cortés, L.V. Besteiro, A. Alabastri, A. Baldi, G. Tagliabue, A. Demetriadou, P. Narang, Challenges in plasmonic catalysis, ACS Nano 14 (2020) 16202–16219, https://doi.org/10.1021/acsnano.0c08773.
[33] G. Baffou, F. Cichos, R. Quidant, Applications and challenges of thermoplasmonics, Nat. Mater. 19 (2020) 1–13, https://doi.org/10.1038/s41563-020-0740-6.
[34] A.V. Kildishev, A. Boltasseva, V.M. Shalaev, Planar photonics with metasurfaces, Science 339 (2013), 1232009, https://doi.org/10.1126/science.1232009.
[35] N. Yu, F. Capasso, Flat optics with designer metasurfaces, Nat. Mater. 13 (2014) 139–150, https://doi.org/10.1038/nmat3839.
[36] S. Gwo, C.-Y. Wang, H.-Y. Chen, M.-H. Lin, L. Sun, X. Li, W.-L. Chen, Y.-M. Chang, H. Ahn, Plasmonic metasurfaces for nonlinear optics and quantitative SERS, ACS Photonics 3 (2016) 1371–1384, https://doi.org/10.1021/acsphotonics.6b00104.
[37] A.M. Shaltout, V.M. Shalaev, M.L. Brongersma, Spatiotemporal light control with active metasurfaces, Science 364 (2019), eaat3100, https://doi.org/10.1126/science.aat3100.
[38] A.O. Govorov, W. Zhang, T. Skeini, H. Richardson, J. Lee, N.A. Kotov, Gold nanoparticle ensembles as heaters and actuators: melting and collective plasmon resonances, Nanoscale Res. Lett. 1 (2006) 84–90, https://doi.org/10.1007/s11671-006-9015-7.
[39] G. Baffou, P. Berto, E. Bermúdez Ureña, R. Quidant, S. Monneret, J. Polleux, H. Rigneault, Photoinduced heating of nanoparticle arrays, ACS Nano 7 (2013) 6478–6488, https://doi.org/10.1021/nn401924n.
[40] J. Hao, J. Wang, X. Liu, W.J. Padilla, L. Zhou, M. Qiu, High performance optical absorber based on a plasmonic metamaterial, Appl. Phys. Lett. 96 (2010), 251104, https://doi.org/10.1063/1.3442904.
[41] W. Li, U. Guler, N. Kinsey, G.V. Naik, A. Boltasseva, J. Guan, V.M. Shalaev, A. V. Kildishev, Refractory plasmonics with titanium nitride: broadband metamaterial absorber, Adv. Mater. 26 (2014) 7959–7965, https://doi.org/10.1002/adma.201401874.
[42] K. Chaudhuri, M. Alhabeb, Z. Wang, V.M. Shalaev, Y. Gogotsi, A. Boltasseva, Highly broadband absorber using plasmonic titanium carbide (MXene), ACS Photonics 5 (2018) 1115–1122, https://doi.org/10.1021/acsphotonics.7b01439.
[43] G.V. Naik, J.L. Schroeder, X. Ni, A.V. Kildishev, T.D. Sands, A. Boltasseva, Titanium nitride as a plasmonic material for visible and near-infrared wavelengths, Opt. Mater. Express 2 (2012) 478–489, https://doi.org/10.1364/OME.2.000478.
[44] U. Guler, A. Boltasseva, V.M. Shalaev, Refractory plasmonics, Science 344 (2014) 263–264, https://doi.org/10.1126/science.1252722.
[45] P. Patsalas, N. Kalfagiannis, S. Kassavetis, G. Abadias, D.V. Bellas, Ch Lekka, E. Lidorikis, Conductive nitrides: growth principles, optical and electronic properties, and their perspectives in photonics and plasmonics, Mater. Sci. Eng. R Rep. 123 (2018) 1–55, https://doi.org/10.1016/j.mser.2017.11.001.
[46] B.T. Diroll, S. Saha, V.M. Shalaev, A. Boltasseva, R.D. Schaller, Broadband ultrafast dynamics of refractory metals: TiN and ZrN, Adv. Opt. Mater. 8 (2020), 2000652, https://doi.org/10.1002/adom.202000652.
[47] A. Naldoni, Z.A. Kudyshev, L. Mascaretti, S.P. Sarmah, S. Rej, J.P. Froning, O. Tomanec, J.E. Yoo, D. Wang, Š. Kment, T. Montini, P. Fornasiero, V.M. Shalaev, P. Schmuki, A. Boltasseva, R. Zbořil, Solar thermoplasmonic nanofurnace for high-temperature heterogeneous catalysis, Nano Lett. 20 (2020) 3663–3672, https://doi.org/10.1021/acs.nanolett.0c00594.
[48] J.E. Yoo, K. Lee, M. Altomare, E. Selli, P. Schmuki, Self-organized arrays of single-metal catalyst particles in TiO_2 cavities: a highly efficient photocatalytic system, Angew. Chem. Int. Ed. 52 (2013) 7514–7517, https://doi.org/10.1002/anie.201302525.
[49] J.E. Yoo, P. Schmuki, Critical factors in the anodic formation of extremely ordered yitania nanocavities, J. Electrochem. Soc. 166 (2019) C3389–C3398, https://doi.org/10.1149/2.0381911jes.
[50] F. Riboni, N.T. Nguyen, S. So, P. Schmuki, Aligned metal oxide nanotube arrays: key-aspects of anodic TiO_2 nanotube formation and properties, Nanoscale Horiz. 1 (2016) 445–466, https://doi.org/10.1039/C6NH00054A.
[51] R. Yang, C. Zhu, Q. Wei, Z. Du, Investigations on structural, elastic, thermodynamic and electronic properties of TiN, Ti_2N and Ti_3N_2 under high pressure by first-principles, J. Phys. Chem. Solids 98 (2016) 10–19, https://doi.org/10.1016/j.jpcs.2016.05.012.
[52] J.E. Bertie, Z. Lan, Infrared Intensities of Liquids XX: the Intensity of the OH stretching band of liquid water revisited, and the best current values of the optical constants of H_2O(l) at 25°C between 15,000 and 1 cm^{-1}, Appl. Spectrosc. 50 (1996) 1047–1057, https://doi.org/10.1366/0003702963905385.
[53] I. Celanovic, N. Jovanovic, J. Kassakian, Two-dimensional tungsten photonic crystals as selective thermal emitters, Appl. Phys. Lett. 92 (2008), 193101, https://doi.org/10.1063/1.2927484.
[54] V. Rinnerbauer, A. Lenert, D.M. Bierman, Y.X. Yeng, W.R. Chan, R.D. Geil, J. J. Senkevich, J.D. Joannopoulos, E.N. Wang, M. Soljačić, I. Celanovic, Metallic photonic crystal absorber-emitter for efficient spectral control in high-temperature solar thermophotovoltaics, Adv. Energy Mater. 4 (2014), 1400334, https://doi.org/10.1002/aenm.201400334.
[55] E. Traver, R.A. Karaballi, Y.E. Monfared, H. Daurie, G.A. Gagnon, M. Dasog, TiN, ZrN, and HfN nanoparticles on nanoporous aluminum oxide membranes for solar-driven water evaporation and desalination, ACS Appl. Nano Mater. 3 (2020) 2787–2794, https://doi.org/10.1021/acsanm.0c00107.
[56] H. Li, Y. He, Z. Liu, B. Jiang, Y. Huang, A flexible thin-film membrane with broadband Ag@TiO_2 nanoparticle for high-efficiency solar evaporation enhancement, Energy 139 (2017) 210–219, https://doi.org/10.1016/j.energy.2017.07.180.
[57] C.O. Popiel, J. Wojtkowiak, Simple formulas for thermophysical properties of liquid water for heat transfer calculations (from 0°C to 150°C), Heat. Transf. Eng. 19 (1998) 87–101, https://doi.org/10.1080/01457639808939929.

Luca Mascaretti completed his Ph.D. in 2018 at the Department of Energy of Politecnico di Milano, with a thesis related to hierarchical TiO_2 nanostructures for water splitting applications. Since April of 2018 he has been member of the Photoelectrochemistry group at the Regional Center of Advanced Technologies and Materials, Palacký University in Olomouc (Czech Republic). His main activities are related to TiN-based nanostructured materials for plasmonics and solar-energy conversion processes, including photocatalysis and solar steam generation.

Andrea Schirato received his B.Sc. from Politecnico di Milano (PoliMi) and Paris-Sud University, he accomplished cum laude his Double Degree MSc's programme across PoliMi and École Centrale Paris. With research experience across PoliMi, École Centrale Paris and Rice University (Houston, TX), he is currently a Physics Ph.D. candidate across PoliMi and the Italian Institute of Technology (Genoa) under Profs. G. Della Valle and R. Proietti Zaccaria's supervision. His activities mostly focus on theoretical study and numerical modeling of ultrafast nonlinear phenomena driven by hot carriers, including electronic and phononic energy transfer in nanostructured materials and metasurfaces.

Radek Zbořil is the funding director of RCPTM Center at Palacký University in Olomouc, Czech Republic. After Ph.D. study, he underwent several stays, e.g. at University of Delaware and University of Tokyo. He is co-author of ca 500 publications and books published by Springer, Wiley and American Chemical Society. His research is focused on low-dimensional nanomaterials for medicine, energy and environmental technologies. Prof. Zbořil is co-inventor of exceptional nanomaterials including non-metallic 1D conductors (Nature Nanotechnol. 2020), non-metallic 2D magnets (Nat. Commun. 2017), or nanoparticles for nanomedicine (Nature Nanotechnol. 2018). He was awarded as Highly Cited Researcher by Clarivate Analytics (2018–2020).

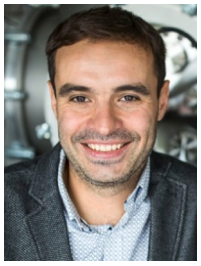

Štěpán Kment received his Ph.D. in solid state physics and photoelectrochemistry in 2010 from Czech Technical University in Prague, Czech Republic. He then spent one year as a postdoctoral research fellow at Department of Electrical Engineering, University of Nebraska – Lincoln, USA. Since 2011 he has been working at the Regional Center of Advanced Technologies and Materials of Palacký University Olomouc, Czech Republic as a Senior Researcher and from 2017 as a head of Photoelectrochemistry group. His research is focused on development of new materials and nanostructures for PEC water splitting application mainly via advanced plasma deposition methods.

Patrik Schmuki is a professor of Materials Science and the head of the Institute of Surface Science at the University of Erlangen-Nuremberg, Germany. He is the recipient of the H.H. Uhlig Award of the NACE, the Volta Award of the Electrochemical Society, and the H. H. Uhlig Award of the Electrochemical Society. He served as the Editor for Encyclopedia of Electrochemistry. His research interests cover electrochemistry and material science at the nanoscale, with a particular focus on functional materials and the control of self-assembly process. He is a Highly Cited Researcher since 2013 with $>$ 700 publications, $>$ 40000 citations (h-index $>$ 100).

Alessandro Alabastri received his BSc and MSc in Engineering Physics from Politecnico di Milano and the Ph.D. in Nanosciences from the Italian Institute of Technology and the University of Genoa. Since 2020, he is Assistant Professor in the Electrical and Computer Engineering department at Rice University. He worked on several aspects of light-to-heat conversion, exploring the mechanisms to maximize heat dissipation in nanoparticle-based systems. He has realized predictive models of light-driven energy conversion systems such as Photon Enhanced Thermionic Emission devices in collaboration with the European Space Agency and Nanophotonics Enabled Solar Membrane Distillation modules at Rice University.

Alberto Naldoni is co-leader of the photoelectrochemistry group at the Regional Center of Advanced Technologies and Materials of Palacký University Olomouc. He obtained his Ph. D. (2010) in Chemical Sciences from University of Milan before moving to the Italian National Research Council to study photocatalysis and photoelectrochemical water splitting. He spent three years as visiting faculty in the Nanophotonics group at the Birck Nanotechnology Center of Purdue University. His research interests focus on solar energy conversion with emphasis on plasmonics, photocatalysis and photoelectrochemistry.